ANALYSIS OF THE BOUNDARY LAYER STABILITY TO ASSESS FLOW SEPARATION CONTROL CAPABILITY IN LOW-PRESSURE TURBINES

7TH EUROPEAN CONFERENCE ON COMPUTATIONAL FLUID DYNAMICS (ECFD 7)

(ECCM –ECFD 2018 CONFERENCE)

IVÁN PADILLA[1], JORGE SAAVEDRA[1,2], GUILLERMO PANIAGUA[1,2] AND FABIO PINNA[1]

[1]Aeronautics and Aerospace Department, von Karman Institute for Fluid Dynamics,
Chaussée de Waterloo 72, 1640 Rhode-Saint-Genèse, Belgium
ivan.padilla@vki.ac.be; fabio.pinna@vki.ac.be

[2]Maurice J. Zucrow Laboratories, Purdue University,
500 Allison Road, West Lafayette, IN, 47907
saavedra@purdue.edu; gpaniagua@purdue.edu

Key words: Boundary Layer, Stability, Flow Separation Control, Low-Pressure Turbine.

Abstract. The stability characteristics of the boundary layer developing over a wall-mounted hump are analysed by means of one-dimensional linear stability theory. The flow field around the hump geometry reproduces the behaviour encountered in the rear suction side of low-pressure turbines, which features flow separation at low Reynolds numbers, significantly reducing turbine efficiency. By employing a time-averaged base flow obtained from laminar Navier-Stokes simulations, linear stability calculations are performed along different streamwise locations. An unstable disturbance is identified developing inside the boundary layer in a small region prior to flow separation. By extending the analysis to different frequencies, the most unstable frequency is also determined, which dominates the complete instability region. The characterization of the most unstable location and frequency provides the necessary data to perform an effective boundary layer tripping to promote the transition to turbulence and reduce flow separation.

1 INTRODUCTION

The advancement of the aerospace industry towards the development of more compact and versatile distributed-thrust power plants is constrained by the occurrence of flow separation in low-pressure turbine airfoils operating at high altitudes. At low Reynolds numbers (in the order of $Re < 10^6$, based on airfoil chord), the rear part of the suction side of the turbine airfoil can suffer flow separation, which increases viscous loses and significantly abates the turbine efficiency [1, 2]. Therefore, the presence of this phenomenon limits the lowest Reynolds number of engine operation, preventing the flight at higher altitudes and ultimately

reducing the flight envelope. With the purpose of boosting turbine performance at low Reynolds numbers, both passive and active flow separation control strategies have been developed [3].

Passive control techniques are mainly based on the use of geometrical elements to promote laminar to turbulent boundary layer transition, i.e. boundary layer tripping, as turbulent boundary layers are more resistant to detachment than those in laminar regime. For instance, Lake and co-authors [4] introduced the use of surface dimples, while Volino [5] studied the effect of using rectangular trips on the suction side, in both cases promoting transition to turbulence to delay separation and encourage flow reattachment. Without focusing on boundary layer tripping, Byerley et al. [6] proposed the use of Gurney flaps for controlling the laminar flow separation on turbine blades. By mounting the flaps near the training edge of the pressure side, the flow is forced to turn and accelerate through the internal passage directing it towards the suction side, where it reduces the adverse pressure gradient that triggers separation at low Reynolds conditions. Passive devices are able to provide a satisfactory control in numerous configurations. However, they usually also have a strong impact in turbine performance at higher Reynolds numbers, reducing performance at lower altitudes. Therefore, low Reynolds tailored turbine designs may prove to be inefficient during take-off, climb and landing operations.

On the other hand, active flow control methodologies offer a much more flexible approach, without any impact on turbine performance when operating at higher Reynolds numbers. A summary of different periodic excitation methods for controlling flow separation is provided by Greenblatt & Wygnanski [7], ranging from approaches based on acoustic waves to boundary layer suction and ingestion. Single dielectric barrier discharge (DBD) plasma actuators have also been widely used for the suppression of flow separation. Huang et al. [8] employed DBD actuators in a linear cascade with effective results. Similarly, Göksel and co-workers [9] looked into the impact on efficiency caused by the use of pulsed plasma actuators at different Reynolds numbers. The lower the Reynolds number, the more effective the control achieved.

An accurate prediction of transition onset is fundamental to perform effective flow control towards the abatement of separation. Nowadays, linear stability theory is progressively consolidating as a practical tool to predict transition in real-world applications [10, 11]. In the context of laminar boundary layer separation, it can be applied to estimate the optimal flow control locations based on a pure theoretical approach, without the need to rely on empirical correlations.

In this work the stability of the boundary layer developing over a wall-mounted hump geometry is analysed by means of linear stability theory. The hump geometry considered induces a flow field that mimics the flow behaviour encountered on the suction side of a low-pressure turbine airfoil, where boundary layer detachment occurs at low Reynolds numbers while no separation takes place for high Reynolds numbers. The shape of the hump is designed using a Bézier curve, which provides a smooth and continuous geometry that does not impose any constraint in the location of the flow separation region, allowing it to be fully governed by the flow similarity parameters. Linear stability calculations are performed on a base flow at a low Reynolds number obtained by means of a laminar Navier-Stokes numerical solution. The instabilities developing in the boundary layer prior to flow separation are identified and characterized over a range of different frequencies. This information allows the

identification of the most favourable region to disturb the boundary layer as well as the optimal actuation frequency to effectively trigger transition and reduce flow separation.

2 GOVERNING EQUATIONS

The governing equations employed in this study are the Navier-Stokes equations for a two-dimensional Newtonian fluid. No assumptions are made regarding the compressibility of the fluid, so the full system of equations is considered. The primitive flow variables are density ρ, pressure p, temperature T and velocity u_i, with $i = 1, 2$. In a Cartesian frame of reference, the conservation form of the equations can be expressed as

$$\frac{\partial \rho}{\partial t} + \frac{\partial (\rho u_i)}{\partial x_i} = 0, \tag{1}$$

$$\frac{\partial (\rho u_i)}{\partial t} + \frac{\partial (\rho u_i u_j)}{\partial x_j} + \frac{\partial p}{\partial x_i} - \frac{\partial \tau_{ij}}{\partial x_j} = 0, \tag{2}$$

$$\frac{\partial (\rho E)}{\partial t} + \frac{\partial (\rho E u_i + p u_i)}{\partial x_i} + \frac{\partial q_i}{\partial x_i} - \frac{\partial (u_i \tau_{ij})}{\partial x_j} = 0, \tag{3}$$

where t is the time coordinate and x_i is the ith spatial coordinate. The viscous stress tensor τ_{ij} satisfies the following relationship

$$\tau_{ij} = \mu \left(\frac{\partial u_i}{\partial x_j} + \frac{\partial u_j}{\partial x_i} - \frac{2}{3} \frac{\partial u_k}{\partial x_k} \delta_{ij} \right), \tag{4}$$

in which μ is the dynamic viscosity of the fluid and δ_{ij} is the Kronecker delta. The total energy of the fluid, denoted by E, is defined as $E = e + u_i u_i / 2$, with e being the specific internal energy. The conductive heat flux vector q_i is related to the fluid temperature by means of Fourier's law, given by $q_i = -k \, \partial T / \partial x_i$, where k denotes the thermal conductivity of the fluid. Assuming a calorically perfect gas, the internal energy of the fluid is defined as $e = c_v T$, with c_v denoting the specific heat at constant volume, which can be directly determined from the specific gas constant R and the ratio of specific heats $\gamma = c_p / c_v$ using $c_v = R / (\gamma - 1)$. Standard values for air are considered, namely, $R = 287.18$ J/(kg·K) and $\gamma = 1.4$. The system is closed through the perfect gas equation of state, expressed as $p = \rho R T$. Sutherland's law is employed to model the variation of the dynamic viscosity with temperature:

$$\mu = \mu_{ref} \left(\frac{T}{T_{ref}} \right)^{3/2} \left(\frac{T_{ref} + S_\mu}{T + S_\mu} \right), \tag{5}$$

where S_μ is the Sutherland temperature constant and μ_{ref}, T_{ref} are respectively the reference dynamic viscosity and static temperature. In the numerical results presented in this work the following values are used: $\mu_{ref} = 1.716 \times 10^{-5}$ kg/(m·s), $T_{ref} = 273.11$ K and $S_\mu = 111$ K. The same law is also employed to take into account the variation of thermal conductivity with temperature, in this case with the parameters $k_{ref} = 2.41 \times 10^{-2}$ W/(m·K) and $S_k = 194$ K at

the same reference temperature.

2.1 Formulation of the one-dimensional linear stability problem

The stability analysis performed in this work is based on classical linear stability theory (LST) [12]. The instantaneous flow field $\mathbf{q} = [u, v, T, p]^T$ is split into a steady reference state $\overline{\mathbf{q}}$, also known as base flow, and a small unsteady perturbation field $\widetilde{\mathbf{q}}$:

$$\mathbf{q} = \overline{\mathbf{q}} + \epsilon\widetilde{\mathbf{q}}, \tag{6}$$

with $\epsilon \ll 1$. The base flow is also assumed to be locally parallel in the streamwise (x) direction, so that $\overline{\mathbf{q}} = \overline{\mathbf{q}}(y)$ at a given x station. Since the base flow is two-dimensional, the amplitude of the perturbations is a function of the wall-normal (y) coordinate only, and homogeneity is imposed in the spanwise (z) and streamwise (x) spatial directions and in time. For this configuration, the ansatz describing the perturbations takes the form

$$\widetilde{\mathbf{q}} = \widehat{\mathbf{q}}(y) \exp[i(\alpha x + \beta z - \omega t)] + c.c., \tag{7}$$

where $\widehat{\mathbf{q}}$ is the one-dimensional amplitude function, α and β are respectively the wavenumbers along the streamwise and spanwise directions, ω is the angular frequency and $c.c.$ denotes the complex conjugate. In this study the interest lies in the spatial evolution of the perturbations along the streamwise direction, hence a spatial stability approach is adopted. The temporal frequency ω and the spanwise wavenumber β are fixed to real values, whereas α is a complex number, $\alpha = \alpha_r + i\alpha_i$. The real part (α_r) represents the streamwise wavenumber of the perturbation and the imaginary part (α_i) its spatial growth rate.

The governing equations of the linear stability problem are obtained by substituting the splitting given by equation (6) into the full Navier-Stokes system (equations (1) to (3)), making use of the ansatz in equation (7) and neglecting the nonlinear terms, namely, the terms of order $O(\epsilon^2)$ or higher. The resulting system of linear differential equations can then be expressed in the following matrix form

$$\mathbf{A}\widehat{\mathbf{q}} = \alpha\mathbf{B}\widehat{\mathbf{q}} + \alpha^2\mathbf{C}\widehat{\mathbf{q}}, \tag{8}$$

where $\mathbf{A}$, $\mathbf{B}$ and $\mathbf{C}$ are complex differential matrix operators. Their specific structure is provided for instance in the study of Pinna [13]. To improve the conditioning of the system, the equations are made nondimensional by introducing the following dimensionless quantities

$$t^* = \frac{tu_e}{l}, \qquad x_i^* = \frac{x_i}{l}, \qquad \rho^* = \frac{\rho}{\rho_e}, \qquad u_i^* = \frac{u_i}{u_e},$$

$$p^* = \frac{p}{\rho_e u_e^2}, \qquad E^* = \frac{E}{u_e^2}, \qquad T^* = \frac{T}{T_e}, \qquad \mu^* = \frac{\mu}{\mu_e}, \qquad k^* = \frac{k}{k_e}, \tag{9}$$

in which the subscript e denotes the boundary layer edge properties, used as reference quantities for the nondimensionalization. The parameter l is the Blasius length scale evaluated at the streamwise position where the stability problem is solved, given by $l = \sqrt{\mu_e s/\rho_e u_e}$. In this definition, the coordinate s is the integrated streamwise distance along the body surface associated to a given streamwise location x, also known as arc length.

The discretization of equation (8) leads to an algebraic generalized eigenvalue problem (GEVP) which is nonlinear in the eigenvalue α. Its linearization is achieved by introducing

the following auxiliary vector: $\hat{\mathbf{q}}^+ = [\hat{u}, \hat{v}, \hat{T}, \hat{p}, \alpha\hat{u}, \alpha\hat{v}, \alpha\hat{T}, \alpha\hat{p}]^T$, so that the problem becomes

$$\mathbf{A}^+\hat{\mathbf{q}}^+ = \alpha\mathbf{B}^+\hat{\mathbf{q}}^+, \tag{10}$$

with

$$\mathbf{A}^+ = \begin{bmatrix} \mathbf{A} & -\mathbf{B} \\ \mathbf{0} & \mathbf{I} \end{bmatrix} \quad \text{and} \quad \mathbf{B}^+ = \begin{bmatrix} \mathbf{0} & \mathbf{C} \\ \mathbf{I} & \mathbf{0} \end{bmatrix}, \tag{11}$$

where $\mathbf{I}$ is the identity matrix. This linearization procedure is known as the matrix companion method [14]. It is important to bear in mind that it duplicates the size of the system to be solved.

3 NUMERICAL METHODOLOGY

3.1 Calculation of the base flow

The computational domain of the problem under study is represented in Figure 1. The geometry of interest is the wall-mounted hump shown in the bottom surface of the domain. The hump is defined by a Bézier curve that ensures a continuous and smooth surface. This geometry reproduces the physical behaviour of the flow field in the rear suction side of a low-pressure turbine, which features flow separation at low Reynolds numbers. The use of such a geometry is advantageous for performing fundamental studies. On one side the fact of being a wall-mounted geometry is convenient for experimental analyses in a linear test section, on the other, the smooth surface ensures that the dynamics of the flow separation are not altered by any geometrical discontinuities, such as the case of a backward facing step, allowing the flow behaviour to be fully governed by the flow similarity parameters. For comparison against future experimental studies, the dimensions of the computational domain coincide with the size of the linear test section at the Purdue Experimental Turbine Aerothermal Laboratory wind tunnel facility [15]. As a result, both the top and bottom surfaces of the domain are treated as isothermal walls at room temperature.

The inflow conditions considered for the numerical solution are summarized in Table 1. They are completely defined by fixing the total pressure (p_0) and total temperature (T_0) at the domain inlet and the static pressure at the domain outlet (p_{out}). For the sake of clarity, the associated freestream Mach number (M_∞) and static temperature (T_∞) that would be achieved in an external flow at the same stagnation conditions are also provided, estimated by means of the flow relations $p_0/p_\infty = [1 + 0.5(\gamma - 1)M_\infty^2]^{\gamma/\gamma-1}$ and $T_0/T_\infty = 1 + 0.5(\gamma - 1)M_\infty^2$ with $p_\infty = p_{out}$. Additionally, the corresponding freestream unit Reynolds number (Re_∞/l) is also shown.

Table 1: Inflow conditions for the numerical solution of the base flow.

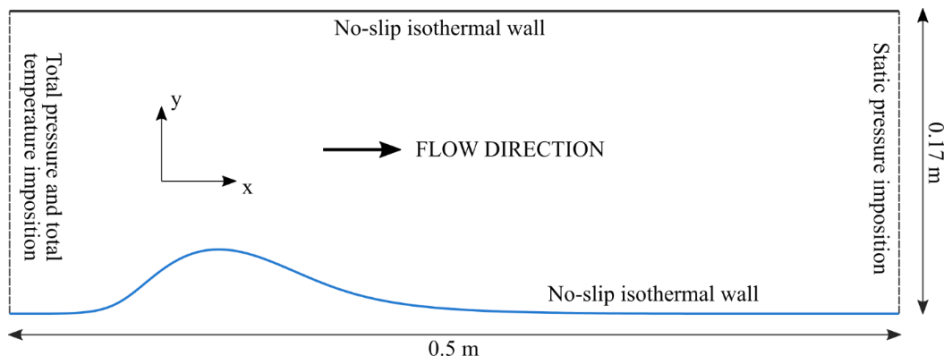| p_0 [Pa]	T_0 [K]	p_{out} [Pa]	M_∞	T_∞ [K]	Re_∞/l [1/m]
101710	500	101325	0.074	499.46	8.73×10^5

Figure 1: Representation of the computational domain and boundary conditions employed for obtaining the numerical solution of the base flow. The hump geometry is shown in blue, corresponding to the bottom boundary.

The two-dimensional numerical solution of the base flow needed for the stability analysis is carried out by means of an unsteady and laminar simulation of the full Navier-Stokes equations, using the commercial CFD package CFD++ and employing a block-structured grid consisting of quadrilateral cells. An unsteady solver is considered to account for the unsteady wake induced downstream of the hump when flow separation is present. The spatial discretization is based on a second-order upwind finite volume scheme, whereas time integration is performed using a second-order implicit scheme with multigrid acceleration. The solution is integrated in time with a time step of $\Delta t = 0.001$ s until the time-averaged residual converges to a constant value.

The boundary conditions of the numerical setup are also shown in Figure 1. At the top and bottom boundaries a no-slip isothermal wall boundary condition is enforced, with a wall temperature of $T_w = 300$ K. At the inlet of the domain, stagnation conditions are imposed by fixing the total pressure (p_0) and the total temperature (T_0). Finally, at the domain outlet the static pressure (p_{out}) is imposed by means of a pressure outlet boundary condition. With respect to the initial conditions, all the flow field is initialized with the freestream values given in Table 1. It is important to note that even if the inflow Mach number is very low, the temperature gradient imposed due to the difference between the freestream temperature and the wall temperature can generate a significant density variation across the boundary layer. For this reason, the full compressible Navier-Stokes equations are considered for this problem.

To ensure a proper resolution of the base flow needed for the stability analysis, well-resolved boundary layer profiles have to be extracted from the CFD solution. To avoid the need for interpolation of the results, a computational grid normal to the wall along the hump surface was designed. The control of every mesh line in the wall-normal direction was achieved by scripting the mesh generation software GAMBIT. To achieve a good resolution of the boundary layer while maintaining a reasonable computational effort, the grid is linearly stretched towards the wall, both in the top and bottom boundaries. The final grid used for the base flow solution has a first cell height of 4.26×10^{-6} m, which ensures that $y^+ < 1$ in all the domain. The number of cells in the wall-normal direction is 1000 while for the horizontal direction 1500 cells are employed, resulting in a total count of 1.5 million cells.
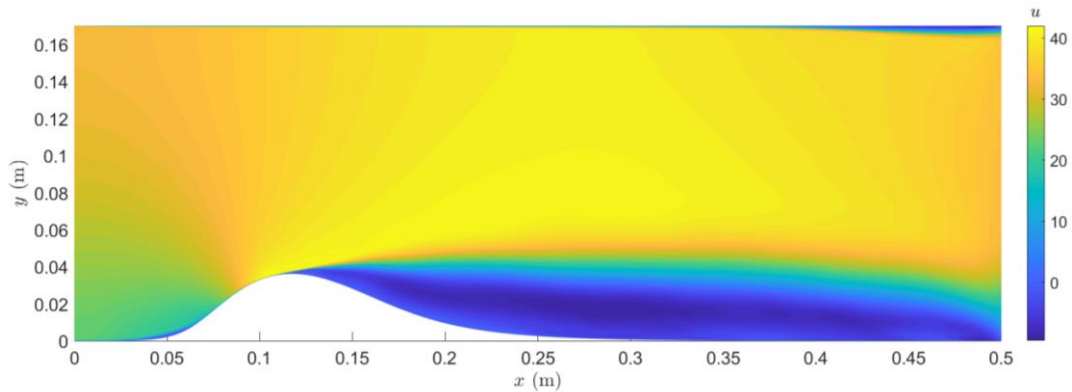
Figure 2: Time-averaged streamwise velocity contours of the obtained base flow solution.

3.2 Solution of the linear stability problem

The solution of the generalized eigenvalue problem (equation (12)) resulting from the linear stability formulation is carried out by means of the von Karman Institute Extensible Stability & Transition Analysis (VESTA) toolkit [16]. The structure of the matrices **A**, **B** and **C** is automatically derived and implemented in MATLAB for each particular configuration using the Maxima computer algebra system. The discretization of the system is achieved using the Chebyshev collocation method, which provides spectral-like accuracy. This technique is based on a Lagrange polynomial interpolation in a nonuniform structured grid given by the Chebyshev-Gauss-Lobatto collocation points. The computational domain for the one-dimensional stability analysis considered here is a wall-normal line containing the discrete boundary layer profile at any specific streamwise location. However, the collocation points are defined on a transformed domain with a wall-normal coordinate $\eta \in$ [1, -1], which does not coincide with the geometrical configuration under study. As a result, an appropriate mapping technique has to be employed in order to transform the set of collocation points to the physical domain. In this case, the classical mapping originally introduced by Malik [17] is applied, which allows the division of the stability domain into two regions, placing half of the collocation points in each of them. Denoting the local wall-normal coordinate by y_n, the transformation can be expressed as

$$y_n = \frac{y_{n,i} y_{n,max} (1 + \eta)}{y_{n,max} - \eta(y_{n,max} - 2y_{n,i})},$$ (12)

where $y_{n,max}$ is the maximum coordinate of the stability domain and $y_{n,i}$ is the coordinate where the number of discrete points is split in half.

To complete the definition of the discrete GEVP, boundary conditions must be imposed on the amplitude of the perturbations $\hat{\mathbf{q}}$. At the wall, the disturbances are forced to satisfy the no-slip condition by setting the velocity perturbations equal to zero. This is accomplished by means of a homogeneous Dirichlet boundary condition. The temperature disturbance at the wall is also imposed to be zero, whereas the pressure perturbation is determined with a compatibility condition based on the wall-normal momentum equation at $y_n = 0$. In the wall-

normal far-field boundary, that is $y_n = y_{n,max}$, the perturbations are forced to decay by imposing once again homogeneous Dirichlet boundary conditions on $\hat{u}$, $\hat{v}$ and $\hat{T}$ and a compatibility condition on $\hat{p}$.

The numerical method used to solve for all the eigenvalues and eigenvectors of the problem is the classical QZ algorithm. This algorithm has a reasonable computational cost for solving the one-dimensional stability problem at one specific location and frequency. Nevertheless, it becomes expensive for studying the evolution of the instability modes at different positions and for a range of different frequencies. For this purpose, a local eigenvalue solver is used, based on the Newton-Raphson iterative algorithm, which tracks the evolution of a single mode along a desired range of conditions. A description of the current solver implemented in VESTA toolkit as well as different validation cases can be found in the work of Pinna [13].

4 RESULTS

Under the configuration described in section 3.1, the numerical solution of the problem reveals that the flow undergoes separation at the chosen Reynolds number, leading to an unsteady wake behind the hump. Although the flow field upstream of the detachment does not present significant changes with time, linear stability theory assumes a steady base flow. For this reason, a time-averaged solution is computed using 400 different time steps after the averaged residual converges to constant value. The resulting time-averaged solution is depicted in Figure 2, which shows contours of streamwise velocity u. This solution was obtained with the computational grid described in section 3.1. As it can be observed, as the flow reaches the beginning of the hump, a small recirculation region appears around $x = 0.05$ m due to the blockage induced by the geometry. Next, the flow accelerates all the way up until reaching the top of the hump, where an adverse pressure gradient is encountered that leads to flow separation. The flow remains separated downstream for remaining portion of the computational domain. The flow separation location is estimated from the skin friction coefficient c_f at the hump wall, when $c_f \approx 0$. For the conditions investigated here, the separation inception takes place at $x \approx 0.1101$ m ($s \approx 0.1198$ m).

4.1 Linear stability analysis

Recalling the methodology described in section 3.2, linear stability calculations are performed in the flow-field prior to boundary layer detachment. The boundary layer profiles at each desired location are extracted from the base flow solution in the wall-normal mesh and nondimensionalized as described in section 2.1. The reference quantities for nondimensionalization are obtained from a numerical solution of the inviscid flow field, which is accomplished by solving the Euler equations, once again using the software CFD++. Following the classical approach in boundary layer theory, the boundary layer edge properties at each streamwise location are assumed to be the wall values computed from the inviscid solution. The stability domain has a height of $y_{n,max} = 0.025$ m to ensure that the upper boundary is far enough for the perturbations to decay to zero. Regarding the mapping parameter $y_{n,i}$, it is locally chosen such that half of the discretization points are placed below a 75% of the boundary layer thickness. This is achieved by imposing $y_{n,i} = 0.75\delta_{99}$, where
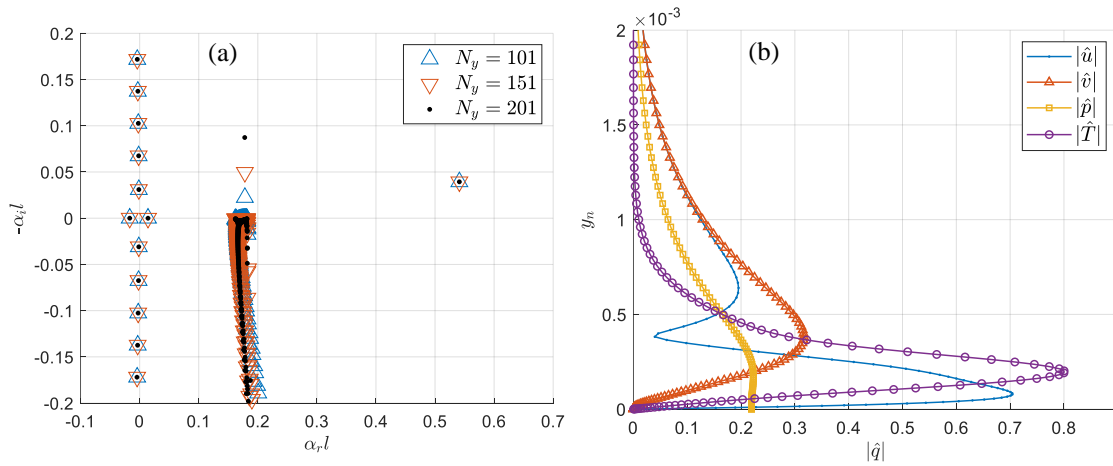
Figure 3: (a) Spatial stability spectrum obtained at $x = 0.1091$ m and $f = 4$ kHz. (b) Magnitude of the amplitude functions for the most unstable mode identified (case with $N_y = 151$).

δ_{99} is the local boundary layer thickness, determined by means of the total enthalpy (H) when $H/H_e = 0.995$, with $H_e = c_p T_0$.

Due to the favourable pressure gradient that characterizes the acceleration region, the boundary layer remains stable for most of the distance along the hump surface. However, an instability has been identified in a small region upstream of the separation point. The exact location depends on the frequency considered, as will be shown later. On first place, the result of the stability calculation at one location and frequency inside the unstable region is presented, with the purpose of illustrating the topology of the spectrum and the associated amplitude functions. Figure 3(a) shows the spatial stability spectrum obtained at $x = 0.1091$ m and at a frequency of $f = 4$ kHz when assuming two-dimensional perturbations, i.e. $\beta = 0$. Different grid resolutions N_y were tested to check for grid convergence and identify the location of continuous, discrete and spurious numerical modes. Two different discretized vertical continuous branches can be observed, one of them located at $\alpha_r l = 0$ (poorly resolved in the current figure scale) and another one at $\alpha_r l \approx 0.2$. These branches are a characteristic feature of the stability domain. According to Balakumar and Malik [18], the branch at $\alpha_r l \approx 0.2$ is associated with vorticity waves whereas the branch along the imaginary axis represents acoustic waves. A spurious mode can also be observed on top of the continuous vertical branch that begins at the real axis, which does not show any grid convergence. This mode is of purely numerical nature and is associated to the discretization error inherent to the numerical scheme in use.

The physically interesting information corresponds to the discrete modes. In this case, a single unstable discrete mode is retrieved, clearly visible at $\alpha_r l \approx 0.53$, which is fully converged with N_y. Figure 3(b) displays the amplitude functions of the different perturbation variables associated with the identified unstable discrete mode. A strong similarity is obtained with the signature amplitude shape of Tollmien-Schlichting waves [19], which constitute the natural instability mechanism developing in the linear stage of the transition process for flat plate boundary layers. It is also interesting to note that the amplitude of the temperature perturbation ($\hat{T}$) is of the same order of magnitude as the one of the streamwise velocity perturbation ($\hat{u}$), reflecting the strong impact of the temperature gradient in the base flow and
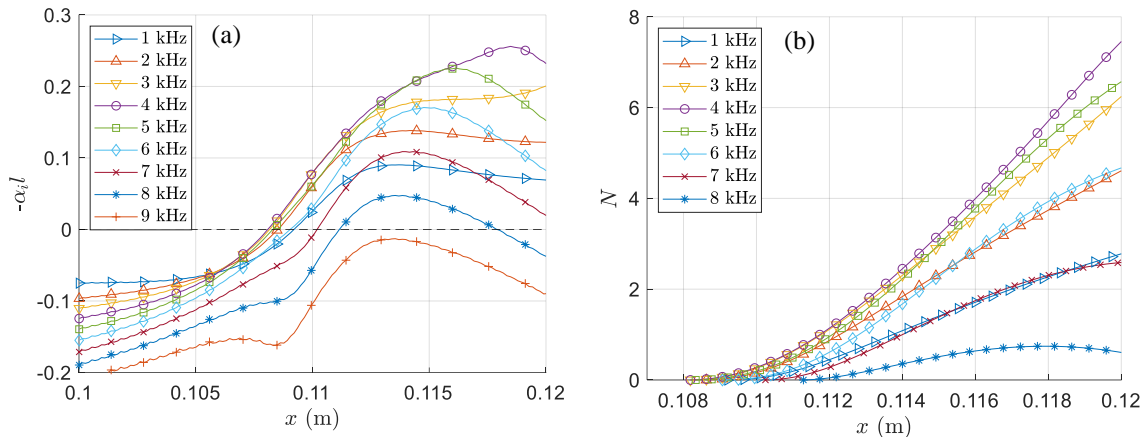
9

Figure 4: (a) Evolution of the growth rate of the least stable mode along $x \in [0.1, 0.12]$ m for different frequencies in the range $f \in [1, 9]$ kHz. (b) Associated integrated logarithmic amplification factors (N-factors).

highlighting the importance of analysing this problem with the compressible Navier-Stokes equations. Different values of β were also tested to assess the behaviour of three-dimensional disturbances. However, at all the conditions investigated the most unstable modes were obtained for $\beta = 0$. This is in agreement with Squire's theorem [19], which states that for incompressible shear flows the most unstable disturbances are always two-dimensional. This is not a surprising result given that the inflow conditions considered here lead to a low-speed flow.

To characterize the boundary layer instability for the problem under study, the streamwise evolution of the identified instability mode is analysed by means of the local stability algorithm for a range of different frequencies. This information allows the computation of the integrated logarithmic amplification rate (N-factor) for each frequency, defined as

$$N = \int_{s_0}^{s} -\alpha_i \, ds, \tag{13}$$

where s_0 is the first location at which the perturbations become unstable, i.e. immediately after crossing the neutral stability curve. This data can then be used to obtain the N-factor envelope curve, employed for transition prediction in the so-called e^N method [20]. Figures 4(a) and 4(b) respectively show the evolution of the growth rate and the computed N-factors for the least stable mode along the region $x \in [0.1, 0.12]$ m ($s \in [0.1093, 0.1296]$ m) and for different frequencies in the range $f \in [1, 9]$ kHz. The final location investigated, $x = 0.12$ m, has been chosen according to the fact that further downstream the boundary layer is fully detached and the stability approach employed in this work is not able to provide physically meaningful results. On the other side, $\beta = 0$ is once again considered. As it can be observed, the boundary layer is initially stable at all the studied frequencies. Then, the growth rate progressively increases at different rates for each frequency, eventually becoming unstable for all the frequencies examined below 9 kHz. The most unstable disturbance is obtained for $f = 4$ kHz. For these conditions, the boundary layer becomes unstable around $x \approx 0.1081$ m, which is before the starting point of separation. This frequency also delivers the highest N-

factor for all the region under analysis, reaching a value of $N \approx 7.8$. As a result, a frequency of $f = 4$ kHz should be the choice for introducing a disturbance inside the boundary layer in the region examined. For the tripping to as effective as possible, the trip location should be placed somewhere between $x \approx 0.1081$ m and $x \approx 0.1185$ m, which is the range for which the mode is unstable and is progressively destabilizing, namely, its growth rate is still growing with x.

5 CONCLUSIONS

The stability characteristics of the boundary layer developing over a wall-mounted hump geometry at low-Reynolds conditions have been investigated by means of one-dimensional linear stability theory (LST). This geometry mimics the flow behaviour encountered in the suction side of low-pressure turbines, where flow separation occurs at low Reynolds numbers, significantly decreasing turbine efficiency. An appropriate control of boundary layer transition can reduce flow separation under such conditions. Linear stability theory provides a purely theoretical approach that can be employed to estimate the location and frequency for performing an optimal boundary layer tripping, necessary for an effective flow separation control based on boundary layer transition.

The base flow needed for the stability analysis was obtained through a laminar and unsteady Navier-Stokes simulation carried out in a wall-normal structured grid. At the conditions considered, the flow field undergoes separation around the top of the hump geometry, producing an unsteady wake downstream. The spatial linear stability calculations performed indicate the presence of an unstable mode growing inside the boundary layer in a small region prior to flow separation. By solving the stability problem at different streamwise locations and frequencies, the optimal actuation location and the most unstable frequency are identified. This frequency is also found to be the dominant frequency for all the streamwise locations investigated.

REFERENCES

[1] Sharma, O. Impact of Reynolds number on low pressure turbine performance. CP-1998-206958, New York, USA. NASA:65-70, (1998).

[2] Hura, H.S., Joseph, J. and Halstead, D.E. Reynolds number effects in a low pressure turbine. ASME GT2012-68501, (2012).

[3] Gad-el-Hak, M. Modern developments in flow control. *Applied Mechanics Reviews* (1996) **49**:365-380.

[4] Lake, J., King, P. and Rivir, R. Reduction of separation losses on a turbine blade with low Reynolds numbers. *Proceedings of the 37th Aerospace Sciences Meeting and Exhibit*, 1999, Reno, Nevada.

[5] Volino, R.J. Passive flow control on low-pressure turbine airfoils. *Transactions of the ASME-T-Journal of Turbomachinery* (2003) **125**(4):754-764.

[6] Byerley, A.R., Störmer, O., Baughn, J.W., Simon, T.W., Van Treuren, K.W. and List, Jr. Using Gurney flaps to control laminar separation on linear cascade blades. *Proceedings of ASME Turbo Expo 2002: Power for Land, Sea and Air*, American Society of Mechanical Engineers, 1191-1199.

[7] Greenblatt, D. and Wygnanski, I.J. The control of flow separation by periodic excitation. *Progress in Aerospace Sciences* (2000) **36**(7):487-545.

[8] Huang, J., Corke, T.C. and Thomas, F.O. Unsteady plasma actuators for separation control of low-pressure turbine blades. *AIAA Journal* (2006) **44**(7):1477-1487.

[9] Göksel, B., Greenblatt, D., Rechenberg, I., Singh, Y., Nayeri, C. and Paschereit, C. Pulsed plasma actuators for separation flow control. *Conference on Turbulence and Interactions TI2006*, May 29-June 2, 2006, Porquerolles, France.

[10] Theofilis, V. Globar linear instability. *Annual Review of Fluid Mechanics* (2011) **43**:319-352.

[11] Zauner, M., Sandham, N.D., Wheeler, A.P.S. and Sandberg, R.D. Linear stability prediction of vortex structures on high pressure turbine blades. *International Journal of Turbomachinery, Propulsion and Power* (2017) **2**(8):1-9.

[12] Mack, L.M. Boundary-layer linear stability theory. Technical report, AGARD-R-709, (1984).

[13] Pinna, F. *Numerical study of stability of flows from low to high Mach number*. PhD thesis, Universitá "La Sapienza" di Roma and von Karman Institute for Fluid Dynamics, (2012).

[14] Bridges, T. and Morris, P. Differential eigenvalue problems in which the parameter appears nonlinearly. *Journal of Computational Physics* (1984) **55**:437-460.

[15] Paniagua, G., Cuadrado, D., Saavedra, J., Andreoli, V., Meyer, T., Meyer, S. and Lawrence, D. Design of the Purdue Experimental Turbine Aerothermal Laboratory for optical and surface aero-thermal measurements. *Proceedings of ASME Turbo Expo 2016: Turbomachinery Technical Conference and Exposition*, June 13-17, 2016, Seoul, South Korea. GT2016-58101.

[16] Pinna, F. VESTA toolkit: a software to compute transition and stability of boundary layers. *43rd Fluid Dynamics Conference*, June 24-27, 2013, San Diego, California.

[17] Malik, M.R. Numerical methods for hypersonic boundary layer stability. *Journal of Computational Physics* (1990) **86**(2):376-413.

[18] Balakumar, P. and Malik, M.R. Discrete modes and continuous spectra in supersonic boundary layers. *Journal of Fluid Mechanics* (1992) **239**:631-656.

[19] Schmid, P.J. and Henningson, D.S. *Stability and transition in shear flows*. Springer, 2001.

[20] van Ingen, J.L. The e^N method for transition prediction. Historical review of work at TU Delft. *38th Fluid Dynamics Conference and Exhibit*, June 23-26 2008, Seattle, Washington.